Multiple structural defects in ultrathin NiFe-LDH nanosheets synergistically and remarkably boost water oxidation reaction

Zhong-Yin Zhao[1], Qi Shao[1], Jiang-Yan Xue[1], Xiaoqing Huang[1]*, Xiao-Xiao Jiang[1],

Bolong Huang[3]*, Xu-Ran Chen[1], Jian-Ping Lang[1,2]*

[1]College of Chemistry, Chemical Engineering and Materials Science, Soochow University, Suzhou 215123, Jiangsu, P. R. China.

[2]State Key Laboratory of Organometallic Chemistry, Shanghai Institute of Organic Chemistry, Chinese Academy of Sciences, Shanghai 200032, P. R. China.

[3]Department of Applied Biology and Chemical Technology, The Hong Kong Polytechnic University, Hung Hom, Kowloon, Hong Kong SAR, P. R. China.

E-mail: hxq006@suda.edu.cnl; bhuang@polyu.edu.hk; jplang@suda.edu.cn

Abstract: Developing highly active, cost-effective and stable electrocatalysts for oxygen evolution reaction (OER) is critical to renewable energy systems. Herein, we demonstrate a H_2O_2-assisted etching method to synthesize mesoporous NiFe layered double hydroxide nanosheets (LDHs) on nickel foam (NF) (NiFe LDHMs/NF). The NiFe LDHMs/NF processed with 200 µL H_2O_2 exhibited excellent OER performance with an extraordinarily low overpotential of 170 mV at 10 mA cm^{-2} in 1 M KOH, as well as superior kinetics with a Tafel slope of 39.3 mV dec^{-1}, being the one of the best non-precious electrocatalysts reported to date. Density functional theory (DFT) calculations revealed that the excellent OER performance arose from pseudo re-oxidized meta-stable Ni^{3+}, which evidently suppressed 3d-e_g of Ni-site and elevated d-band center towards competitively low electron-transfer barrier. The Fe-sites within the system robustly preserved Ni oxidation state and maintained electron-transfer activities. This protocol is applicable to developments of high-efficiency non-precious metal OER electrocatalysts.

Keywords: mesoporous layered double hydroxide nanosheets; oxygen evolution reactions (OER); d-band modulations; noble-metal free

The increasingly global energy crisis and environmental contamination have stimulated intense research on the design of cost-effective and highly active catalysts for electrochemical water splitting, which is a promising way to realize clean and

sustainable energy conversion and storage system [1-5]. However, the electrochemical process is greatly hampered by the unfavorable thermodynamics and inherent sluggish kinetics of the oxygen evolution reaction (OER), owing to the multistep proton-coupled electron transfer and rigid oxygen-oxygen bond formation at a high overpotential [6-8]. Currently, noble-metal oxides (RuO_2 and IrO_2) are the most effective electrocatalysts for OER but still require overpotentials of exceeding 200 mV to drive the current density of 10 mA cm^{-2} [9]. Moreover, the high cost and scarcity of these catalysts limit their large-scale commercial applications. Therefore, significant efforts have been devoted to developing active and durable non-noble OER electrocatalysts based on earth-abundant elements under alkaline conditions, such as first-row (3d) transition metal (TM) oxides 10, layered double hydroxides (LDHs) [11-12], nitrides [13], phosphides [14], and perovskite oxides [15-16].

In recent years, the ultrathin NiFe LDHs nanosheets, as one of the best OER electrocatalysts, have attracted increasing attention due to their unique physical and electronic structures [11,17]. However, their limited specific surface areas and poor electronic conductivity have hindered their further improvement of OER performances and final practical applications [18]. As is well known, catalytic reaction commonly takes place on the surface of the catalysts, which indicates that the electrocatalytic activities of the catalysts strongly depends on their surface nanostructures [19]. According to the previous works, two methods can modify the surface of nanostructures. One general way is to dope a third element into the nanostructure [20, 21], while the other way is to introduce nanopores into the

nanostructure , which may increase the surface area and expose more active sites, and can even shorten electron/ion diffusion path [22, 23]. However, very fewer studies have been reported on the latter strategy due to the formidable experimental difficulty in constructing a new mesoporous structure without changing its compositions. Duan and co-workers reported a graphene nanomesh prepared by using block copolymer lithography, which can open up a bandgap in a large sheet of graphene to enhance electrochemical property [24]. Up to now, the common strategies to fabricate mesoporous electrocatalysts require multiple complicated synthetic steps, which impedes large-scale preparation and application [25]. On the other hand, the electronic structure also plays an important role in the OER process [26]. The regulation of the electronic structures of the catalysts effectively optimizes the adsorption energy of OER intermediates, which could significantly enhance the catalytic activity [27, 28]. Shao-Horn, et al. [6] reported that 3d transition-metal-based electrocatalysts having a surface cation e_g orbital occupancies such as Ni^{3+} ($t_{2g}^6e_g^1$) close to unity can enhance the intrinsic OER activity because of the increased covalency of transition metal-oxygen bonds [29]. Although these results demonstrated the introduction of Ni^{3+} could greatly enhance the performance, Ni^{3+} ($t_{2g}^6e_g^1$) is very difficult to be introduced into Ni-related LDHs including NiFe LDHs nanosheets. To this end, how to precisely construct mesoporous structures of the NiFe LDHs nanosheets and finely tailor the electronic configuration of surface cations by a fast, facile and green way remains a great challenge.

Inspired by the above-mentioned pioneering works by Duan and Shao-Horn, it

would be challenging yet significant to simultaneously create nanopores and introduce of Ni^{3+} on NiFe LDHs nanosheets for high-performance water oxidation. In this paper, we demonstrated a novel and facile approach to prepare ultrathin NiFe LDHs nanosheets on nickel foam (NF) with a free-standing mesoporous structure (denoted as NiFe LDHMs/NF) enriched in Ni^{3+} as a highly efficient electrocatalyst for OER via a H_2O_2 assisted etching strategy. The Ni^{3+}-enriched NiFe LDHMs/NF treated with 200 μL H_2O_2 exhibited excellent OER activity with an extraordinarily low overpotential of 170 mV at 10 mA cm^{-2} and a Tafel slope value of 39.3 mV dec^{-1} in alkaline solution, which is superior to reported NiFe LDHs/NF and outperforms many other state-of-the-art OER catalysts. It also displayed superb long-term durability at a current density of 10 mA cm^{-2} for 45 h. DFT calculations revealed that, competitively high electron-transfer rate originated from the pseudo re-oxidized metal-stable Ni^{3+} within the modified NiFe LDHMs/NF. These electronically active regions locally stabilized the *O preventing active sites being oxidized. Meanwhile, these regions further minimized the intermediating energetic cost with local reconstruction, illustrating the vital function for optimal OER performance. It preliminarily proposed a universal key for optimal OER performance.

Results and Discussion

Preparation and characterization of NiFe LDHMs/NF. The NiFe LDHMs (atomic ratio of Ni and Fe = 3:1) was *in situ* grown on NF through a one-step hydrothermal process accompanied by the formation of nanopores and partial oxidation of Ni^{2+} into

Ni^{3+} using H_2O_2 (**Fig. 1**). In order to investigate the role of the H_2O_2, different amounts of H_2O_2 (20, 60, 200 and 300 μL) were added into 20 mL H_2O containing Ni^{2+}, Fe^{3+}, NH$_4$F and urea. The mixture was sealed in a 50 mL Teflon-lined autoclave and heated at 120℃ for 16 h to yield ultrathin NiFe LDHMs (NiFe LDHMs/NF-20, NiFe LDHMs/NF-60, NiFe LDHMs/NF-200 and NiFe LDHMs/NF-300). Compared with the glaze of NF (**Supplementary Fig. 1**), the scanning electron microscopy (SEM) images showed that the vertically aligned and interconnected nanosheets were uniformly grown on NF (**Fig. 2a, Supplementary Fig. 2a, b and Fig. 3a**), similar to the pristine NiFe LDHs/NF prepared without H_2O_2 (denoted as p-NiFe LDHs/NF) (**Supplementary Fig. 4a, b**). Transmission electron microscopy (TEM) images of the NiFe LDHMs peeled off from NF further revealed that the abundant mesopores could be clearly discerned on the surface of the NiFe LDHMs (**Fig. 2b, c, Supplementary Fig 2c, d**) while the surface of p-NiFe LDHs is quite smooth without mesopores (**Supplementary Fig. 5a, b**), indicating that H_2O_2 played an important role in the formation of the mesoporous structure. By adding H_2O_2, the adsorbed H_2O_2 molecules on the surface of the p-NiFe LDHs can partially oxidize Ni^{2+} into Ni^{3+}, which gradually etched the surface of the p-NiFe LDHs, creating mesopores along the p-NiFe LDHs [30] (**Supplementary Fig. 6**). The mesopore size distribution histograms showed the average mesopore size was enlarged with the increase of the amount of H_2O_2 (**Supplementary Fig. 2e, f and Supplementary Fig. 7a**). Furthermore, excess H_2O_2 would expand pore size greatly so as to destroy the porous structure due to the over-etching in the fabrication process (**Supplementary Fig. 3b,**

c). The energy dispersive X-ray spectroscopy (EDS) spectrums (**Supplementary Fig. 8**) suggested the Ni/Fe ratios of the as-prepared samples were close to 3, which resembled the starting materials. As shown in Fig. 2d, the high-resolution TEM (HRTEM) image of the NiFe LDHMs-200 illustrated the interplanar spacing (012) was amounted to be 0.25 nm, which is the same to that of p-NiFe LDHs (**Supplementary Fig. 5c**). Simultaneously, the corresponding selected electron diffraction (SAED) exhibited two diffraction rings made up of discrete hexagonally arranged spots, which can be indexed to (012) and (110) planes of NiFe LDHMs-200 (**Supplementary Fig. 7b**). The high-angle annular dark-field scanning transmission electron microscopy (HAADF-STEM) image and the energy dispersive X-ray spectroscopy (EDX) mappings (**Fig. 2e and Supplementary Fig. 5d**) suggested that Ni, Fe and O were uniformly distributed in the whole NiFe LDHMs-200 and p-NiFe LDHs. In addition, the thickness of the NiFe LDHMs-200 was determined to be *ca.* 1.86 nm by atomic force microscopy (AFM) (Fig. 2f). The ethanol dispersion of the NiFe LDHMs-200 irradiated with a laser beam displayed the Tyndall phenomenon (**Supplementary Fig. 7c**), indicating the formation of homogeneous ultrathin nanosheets and excellent dispersibility of the NiFe LDHMs-200. The crystal structures of all obtained samples were verified by powder X-ray diffraction (PXRD) (**Fig. 2g and Supplementary Fig. 9**). The well-defined diffraction peaks of the p-NiFe LDHs at 2θ values of 11.9°, 23.7°, 34.7°, 39.3°, 46.5°, 60.2° and 61.5° can be ascribed to the (003), (006), (012), (015), (018), (110) and (113) planes of NiFe LDHs (JCPDS# 51-0463), respectively. Interestingly, no obvious changes were observed in

the PXRD patters of the NiFe LDHMs, indicating the main frameworks were well retained after impregnation using different amounts of H_2O_2.

Owing to the aforementioned structure features, the nitrogen adsorption-desorption isotherms were used to investigate the porous structure of NiFe LDHMs/NF. The Brunauer-Emmett-Teller (BET) surface areas of NiFe LDHMs/NF-200 (**Fig. 3a**) were determined to be 84.7 m^2 g^{-1}, which was 2.72 times larger than that of p-NiFe LDHs/NF (31.1 m^2 g^{-1}). Furthermore, when the amount of H_2O_2 used were 20μL, 60μL and 300μL, respectively, the BET surface areas were determined to be 87.6 m^2 g^{-1}, 85.4 m^2 g^{-1} and 83.2 m^2 g^{-1}, respectively (**Fig. 3d and Supplementary Fig. 10**). No obvious changes were observed in the pore size distribution curves as compared with that of NiFe LDHMs-200/NF. The compositions and chemical valence states of the as-fabricated samples were examined by X-ray photoelectron spectroscopy (XPS). The survey spectra of all the samples confirmed the existence of Ni, Fe and O, being consistent with the EDX results (**Supplementary Fig. 11**). For the high-resolution Ni 2p spectrum of NiFe LDHs/NF-200 (Fig. 3b), the binding energies of Ni $2p_{3/2}$ and Ni $2p_{1/2}$ located at 856.4 eV and 874.0 eV could be ascribed to Ni^{2+}, alongside with shakeup satellites at 862.7 eV and 880.8 eV, respectively [31]. Compared to that of the p-NiFe LDHs/NF, two new peaks centered at 858.1 eV and 876.1 eV could be assigned to the Ni^{3+} species in NiFe LDHMs/NF [32] (**Fig. 3b and Supplementary Fig. 12a**), suggesting that a portion of Ni^{2+} was oxidized into Ni^{3+}. Meanwhile, Ni $2p_{3/2}$ and Ni $2p_{1/2}$ peaks of NiFe LDHMs/NF were both positively shifted to higher binding energies (*ca.* 0.4 eV) compared with that of

p-NiFe LDHs/NF, which is mainly ascribed to the formation of Ni^{3+}. Notably, the ratio of Ni^{3+}/Ni^{2+} on the surface of NiFe LDHMs/NF could be obtained by comparing the fitted curve covered. It was obvious that the ratio of Ni^{3+}/Ni^{2+} on the surface of NiFe LDHMs/NF was increased from 22.19% to 25.97% with the increase of the amount of H_2O_2 from 20 to 200 μL (Fig. 3d and Supplementary Table 1). This result indicated the generation of more oxygen vacancies on the surface of the nanosheets after the H_2O_2 impregnation, which could be further confirmed by the high-resolution O 1s spectrum. However, when the amount of H_2O_2 was further increased up to 300 μL, the ratio of Ni^{3+}/Ni^{2+} on the surface got decreased to 25.77% instead. In the high-resolution O 1s spectrum (Fig. 3c and Supplementary Fig. 12b), p-NiFe LDHs/NF displayed two oxygen peaks whereas NiFe-LDHMs/NF showed three peaks. In detail, the component O_1 at 531.2eV is typical of metal-oxygen bonds [33]. The component O_2 at 531.8eV is attributed to surface oxygen defect/ vacancy species (O_{vac}) [34]. The component O_3 at 532.3eV is corresponding to the hydroxy species of surface-adsorbed water molecules [35]. The absence of the component O_2 in p-NiFe LDHs/NF spectrum indicated that p-NiFe LDHs/NF lack oxygen defects on its surface. The ratio of the area O_{vac}/O ($O_2/O_1+O_2+O_3$) is the highest for NiFe LDHMs/NF-200 among all the samples (Fig. 3d and Supplementary Table 2), which is also consistent with the ratio of Ni^{3+}/Ni^{2+} in the Ni spectrum. In addition, as shown in Fe 2p spectrum (Supplementary Fig. 12c), no obvious changes were observed in all NiFe LDHMs. The two characteristic peaks at 712.3eV and 725.0eV were attributed to Fe $2p_{3/2}$ and Fe $2p_{1/2}$ of Fe^{3+} species. The unique structure of NiFe LDHMs/NF with

predominance of Ni^{3+} may improve the electronic conductivity, create more active sites and thus enhance its OER activity.

Electrocatalytic OER Catalysis. The electrochemical performance of NiFe LDHMs/NF-200 toward OER was evaluated in 1 M KOH solution using a typical three-electrode system operated at 5 mV s^{-1}. For comparison, a set of references were also studied under identical test conditions. All the polarization curves are presented with 95% *iR* compensation and Non-*iR*-corrected polarization curves are given in Supplementary Fig. 13. Bare NF exhibited weak OER activity, suggesting the effect of NF on the overall activity of catalysts was very small (Supplementary Fig. 14). According to the linear sweep voltammetry (LSV), the oxidation peaks located at 1.38 V versus a reference hydrogen electrode (RHE) correspond to the oxidation of Ni^{2+} to Ni^{3+} in all samples (**Fig. 4a**). For the anodic potential, the NiFe LDHMs/NF showed a significantly steeper response at lower potentials after H_2O_2 oxidation treatment, being in contrast to that of the p-NiFe LDHs/NF. In particular, NiFe LDHMs/NF-200 displayed the best OER performance with the onset potential of 1.34 V, which is lower than other samples. Furthermore, as shown in Fig. 4b, with the increase of the amount of H_2O_2 from 0 to 200 μL, the overpotential at the current density of 10 mA cm^{-2} got decreased from 299 mV to 170 mV, thereby revealing the importance of H_2O_2 oxidation in promoting OER activity. However, when the dosage of H_2O_2 was raised up to 300 μL, the overpotential was increased to 186 mV, indicating the excess amount of H_2O_2 reduced the OER activity, which was probably due to the fact that excess H_2O_2 might destroy the porous structure so as to diminish the number of

exposed active sites. The current density of NiFe LDHMs/NF-200 is 80.5 mA cm^{-2} at 1.45 V, which is 40 times, 7.9 times, 5.3 times and 1.4 times higher than those of p-NiFe LDHs/NF (2.0 mA cm^{-2}), NiFe LDHMs/NF-20 (10.1 mA cm^{-2}), NiFe LDHMs/NF-60 (15.2 mA cm^{-2}) and NiFe LDHMs/NF-300 (57.8 mA cm^{-2}), respectively. Such an excellent OER performance of NiFe LDHMs/NF-200 is superior to many non-precious OER electrocatalysts reported previously (**Supplementary Table 3**). In addition, it is interesting to observe the specific activity (current per BET area) of the OER electrocatalysts that can be used to understand the synergetic role of the surface area and Ni^{3+}. After normalizing the current by BET surface area, NiFe LDHMs/NF-200 still exhibited better OER performance than NiFe LDHMs/NF (**Supplementary Fig. 15**), confirming that the enhanced OER performance of NiFe LDHMs/NF can be mainly originated from the intrinsic activity of catalysts rather than only from the BET surface area. The intrinsic activity of NiFe LDHMs/NF can be ascribed to the higher content of Ni^{3+} compared with other NiFe LDHMs/NF, which is helpful to facilitate the OER process.

The catalytic reaction kinetics of the electrocatalysts were studied by Tafel plots (Fig. 4c). The corresponding Tafel slope of NiFe LDHMs/NF-200 was measured to be 39.3 mV dec^{-1}, which is smaller than those of NF (115.64 mV dec^{-1}), p-NiFe LDHs/NF (78.21 mV dec^{-1}), NiFe LDHMs/NF-20 (74.39 mV dec^{-1}), NiFe LDHMs/NF-60 (70.57 mV dec^{-1}) and NiFe LDHMs/NF-300 (42.58 mV dec^{-1}), suggesting a superior OER capability with decreasing overpotentials. Electrochemical impedance spectroscopy (EIS) (**Fig. 4d**) was performed to reveal that NiFe

LDHMs/NF-200 has a smaller charge transfer resistance compared to p-NiFe LDHs/NF, NiFe LDHMs/NF-20, NiFe LDHMs/NF-60 and NiFe LDHMs/NF-300, indicating a faster electron-transfer rate during the OER process. The electrochemical active surface area (ESCA) (**Supplementary Fig. 16**) was also calculated by measuring the cyclic voltammetry (CV) at different scan rates within a non-faradic potential range of 0-0.1V. The capacitance (C_{dl}) of NiFe LDHMs/NF-200 is 9.53 mF cm^{-2}, approximately 2.2 times larger than that of p-NiFe LDHs/NF (4.24 mF cm^{-2}), implying the existence of abundant catalytically active sites. The electrocatalytic durability is another important criterion for evaluating the OER performance of electrocatalysts. After 1000 CV cycles, the CV curve of NiFe LDHMs/NF-200 is nearly identical to the initial one as shown in **Fig. 4e**. Notably, after durability test, SEM and TEM images (**Supplementary Fig. 17**) showed that the morphology and porous structure were maintained. The EDS spectrum (**Supplementary Fig. 18**) of NiFe LDHMs/NF-200 revealed that the Ni : Fe ratio is 19.1 : 6.4, which is similar to the value of 18.0 : 5.8 before test. In addition, the peak positions and relative intensities of Ni 2p, Fe 2p and O1s in their XPS spectra remained essentially unchanged after the OER electrocatalysis (**Supplementary Fig. 19**). Moreover, the long-term electrochemical stability (**Fig. 4f**) of NiFe LDHMs/NF-200 was also conducted at a fixed current density of 10 mA cm^{-2}, revealing that the overpotential retained fairly stable with negligible decay even after 45 h continuous operation. As shown in SEM and TEM images (**Supplementary Fig. 20**), the porous morphology of NiFe LDHMs/NF-200 was well-preserved. All these results confirmed excellent

long-term stability of NiFe LDHMs/NF-200 for OER.

Density functional theory (DFT) calculations were carried out to interpreted mechanism of high OER performance of NiFe LDHMs/NF in the alkaline condition (See computational details). The active bonding and antibonding orbitals near the Fermi level (E_F) have been demonstrated among NiFe-LDHMs/NF (**Supplementary Fig. 21a**), NiFe-LDHMs/NF with O_{vac} formed (**Supplementary Fig. 21b**) and NiFe-LDHMs/NF with re-oxidized Ni near O_{vac}, respectively (**Supplementary Fig. 21c**). Overall, three interface systems have presented evidently spatial electron-transfer within NiFe-LDHMs region. The existence of oxygen vacancies and Ni^{3+} still influences the electronic distributions, especially to the redox turnover character of electronic orbital distribution.

The projected partial density of states (PDOSs) analysis showed the evident suppression of the $3d$-e_g-component of the surface Ni-sites at the surface edge region. The dominant peaks of these t_{2g} components of Ni-$3d$ bands exhibited the upshifting trend towards E_F indicating higher electronic-transfer activity and the valence state, while the e_g-component was suppressed favorably by preparing O-$2p$-π electrons of OH docking at the initial adsorption stage. The Ni-$3d$ center was upshifted from the E_V = -2.0 eV towards E_V = -0.8 eV (E_V = 0 for E_F), denoting higher bonding capability of OH and electron-transfer activity. The formation of oxygen vacancies is the key factor to promote increased concentration of Ni^{3+}, which is supportive of the increased Ni^{3+} concentration characterized by experiments (**Fig. 5a**). The PDOSs analysis of various Fe-sites indicated a nearly pinned feature for the Fe-$3d$ band. The peak positions of the t_{2g} and e_g components have been almost unchanged staying at E_V = -2.6 eV and E_V = +0.6 eV, respectively. This potentially indicated the Fe-sites within

the system played a role of robustly preserving the Ni oxidation states and maintaining electron-transfer activities (**Fig. 5b**). The PDOSs of the adsorbed intermediate O-species were also analyzed. From the adsorbed *OH towards the *O=O, the linear scaling trend of electron-transfer were clearly exhibited and preserved. Especially to the adsorbing *O state, the O-2p-π band is modified across E_F showing substantially high electronic activity (**Fig. 5c**). With NiFe-LDHMs/NF edge modified, the overall work function for various structural configurations were illustrated (**Supplementary Fig. 21d**). It showed an elevated trend of electron-transfer capability from the system towards O-species. Within this trend, the further high oxidation of the Ni site at the O_{vac} edge lowered the electron-transfer barrier via local reconstructions between Ni and Fe sites. The formation of oxygen vacancies not only facilitates the formation of Ni^{3+} but also activates the electroactivity of the region constructed by the pseudo re-oxidized meta-stable Ni^{3+} and oxygen vacancies. Meanwhile, the existence of Ni^{2+} sites also balance the valence states of the meta-stable Ni^{3+} to guarantee stability of the electrocatalysts in long-term applications.

Furthermore, the overall OER pathway on the surfaces of p-NiFe LDHs/NF and NiFe LDHMs/NF with Ni re-oxidized near O_{vac} were calculated. It showed that under $U = 0$ V (standard potential), both systems showed the potential determining step occurring at the same step of forming *OOH. The character originated from the prominent electron-transfer capability of adsorbing *O states at the re-oxidized Ni near O_{vac} instead of low valence Ni-sites (Fig. 5d). At the potential of $U = 1.23$ V, the contrasting energetic evolution was evidently presented. The overbinding of *OH on the p-NiFe LDHs/NF resulted in a higher barrier of forming *O. Meanwhile, the *O

formation was substantially favorable on the NiFe-LDHMs/NF with Ni re-oxidized near O_{vac} (0.02 eV vs -0.07 eV), which resulted in the diversified formation of *OOH+H_2O+OH$^-$ (0.27 eV vs 0.04 eV). Notably, the corresponding barrier level of NiFe LDHMs/NF with Ni re-oxidized near O_{vac} (0.11 eV) showed nearly three times lower than that of the p-NiFe LDHs/NF (0.26 eV). This consistently agreed the experiments that the formation of *O state could obviously alleviate the barrier of stabilizing *OOH and electron-transfer towards high reactivities (**Fig. 5e**). Further structural evolution displayed that the Ni re-oxidized near O_{vac} region not only facilitated the initial facile O-H cleavage but also stabilized *O to further oxidize the *OOH. Therefore, both electronic and energetic properties have been discussed and consistently confirmed the energetically favorable OER performance given by the NiFe LDHMs/NF with Ni re-oxidized near O_{vac}.

According to the careful analysis of the above experimental and theoretical works, the substantially enhanced OER performance of p-NiFe LDHs/NF after H_2O_2 oxidation may be attributed to the following reasons. First, the unique mesoporous structure could not only provide a large surface area, which enables a high interfacial contact with the electrolyte and exposes more active sites, but also accelerates the charge/ion transfer effectively. Second, the abundant Ni^{3+} surface active sites with occupancy of the e_g orbital ($t_{2g}^6 e_g^1$) can accelerate the formation of the hydroperoxyl species that are key intermediates in the evolution of O_2 via the nucleophilic reaction with O [36]. Third, the *in situ* created Ni^{3+} and delocalized electrons on the mesoporous nanosheet surface can dramatically increase the conductivity of p-NiFe

LDHs/NF.

Conclusion

In summary, NiFe LDHMs/NF were successfully prepared by a H_2O_2 assisted etching method. The NiFe LDHMs/NF treated with 200 µL H_2O_2 displayed an outstanding OER activity with an extraordinarily low overpotential of 170 mV at 10 mA cm^{-2} and a small Tafel slope of 39.3 mV dec^{-1} and maintained its catalytic activity for 45 h operation without obvious decay in alkaline media. DFT calculations revealed that, the high oxidation state of Ni at the edge site exhibited high elevated d-band center with e_g-component suppressed. Such scenario uniquely preserved the co-existence of high and low valences of Ni-sites for fast redox rate with lower activation barrier. With this trend, the system not only possessed an electron-active character at the *O state, but also contributed an effective electron-transfer for stabilizing the *OOH. It is a key for optimally minimizing overall OER barriers. This strategy is anticipated to be applicable for creating other non-precious electrocatalysts and open up a fascinating way to develop high-efficiency electrocatalysts for various applications.

Methods

Materials. Nickel (II) chloride hexahydrate ($NiCl_2 \cdot 6H_2O$, AR), iron (III) chloride hexahydrate ($FeCl_3 \cdot 6H_2O$, AR) and ammonium fluoride (NH_4F, AR) were purchased from Sinopharm Chemical Reagent Co. Ltd (Shanghai China). Potassium hydroxide (KOH, 95%) was purchased from Shanghai Aladdin Biochemical Technology Co. Ltd.

Urea ($CO(NH_2)_2$, AR) was purchased from Shanghai Yuanye Bio-Technology Co. Ltd. Hydrogen peroxide (H_2O_2, 30%) was purchased from Shanghai Lingfeng Chemical Reagent Co. Ltd. All the chemicals were used as received without further purification. Deionized water was used throughout the experimental process.

Synthesis of NiFe LDHMs/NF. Typically, a mixture of $NiCl_2 \cdot 6H_2O$ (0.9 mmol), $FeCl_3 \cdot 6H_2O$ (0.3 mmol), urea (8.3 mmol) and NH_4F (3.2 mmol) was dissolved in deionized water (20mL) with continuously stirring to obtain a clear solution. Then H_2O_2 (200 µL) was slowly added dropwise into the above solution. A piece of nickel foam (2.8 cm × 2cm) was cleaned with 6 M HCl solution in an ultrasonic bath for 30 min to remove the surface NiO layer and then rinsed with deionized water, acetone and ethanol. The above mixture solution and nickel foam were transferred into a 50 mL Teflon-lined stainless-steel autoclave and then heated for 16 h at 120 ℃ in a drying oven. After naturally cooling to room temperature, the resulting electrocatalysts (denoted as NiFe LDHMs/NF-200) were washed with deionized water and ethanol three times and dried at 60 ℃ overnight. For comparison, the same procedure used for the preparation of NiFe LDHMs/NF with different amounts of H_2O_2 (0, 20, 60 and 300 µL) were denoted as p-NiFe LDHs/NF, NiFe LDHMs/NF-20, NiFe LDHMs/NF-60 and NiFe LDHMs/NF-300, respectively.

Characterization. Powder X-ray diffraction (XRD) patterns were collected on an X'Pert-Pro MPD diffractometer (Netherlands PANalytical) with a Cu Kα X-ray source (λ = 1.540598 Å). SEM images were performed with a HITACHI S-4700 cold field emission scanning electron microscope operated at 15 kV. Transmission electron

microscopy (TEM), high-resolution TEM (HRTEM), TEM mapping and high-angel annular dark-field scanning TEM (HAADF-STEM) were taken with a FEI Tecnai F20 transmission electron microscope at an acceleration voltage of 200 kV. The thickness of the resulting nanosheets was determined by atomic force microscopy (AFM) with a Dimension Icon (Bruker) AFM system with ScanAsyst. X-ray photoelectron spectrum (XPS) was recorded on an SSI S-Probe XPS Spectrometer. The specific surface areas were calculated through nitrogen adsorption-desorption measurements using the Brunauer-Emmett-Teller (BET) method. The corresponding pore size distributions were obtained by Barrett-Joyner-Halenda (BJH) method.

Electrochemical measurements. All electrochemical measurements were carried out on a CHI 660E electrochemical workstation in a three-electrode system, in which the obtained samples were directly utilized as a working electrode, Ag/AgCl electrode as the reference electrode and a platinum wire as the counter electrode. All potentials measured were converted with respect to reversible hydrogen electrode (RHE) by following the equation: $E_{RHE} = E_{Ag/AgCl} + 0.059$ pH $+ 0.197$ V and overpotential $\eta = E_{RHE}$-1.23 V. Before test, the working electrode was tailored as a square piece with the working surface area of 0.5 cm^{-2}. The polarization curves for OER were obtained by linear voltammetry (LSV) sweeping with a scan rate of 5 mV s^{-1} in 1.0 M KOH medium. The long-term stability was evaluated by a chronoamperometric measurement. Electrochemical active surface areas (ECSA) were measured by cyclic voltammetry (CV) in the potential range of 0-0.1 V versus RHE, with different scan rates of 10, 20, 30, 40 and 50 mV s^{-1}. Electrochemical impedance spectroscopy (EIS)

was surveyed in the frequency range of 100 kHz - 0.01 Hz at 0.52 V versus RHE.

Computational details. The simple density functional theory (DFT) calculations were used based on the CASTEP code [37]. The algorithm of Broyden-Fletcher-Goldfarb-Shannon (BFGS) was chosen for all related geometry optimization calculations. The plane-wave basis set for expressing the valence electronic states was used with a kinetic cutoff energy of 750 eV. The PBE functional was set for the calculations. During electronic-minimization process, the ensemble DFT (EDFT) method of Marzari et al [38] was used to guarantee the convergence and avoid spin-charge sloshing effect.

Regarding the interface structural model with bonding form, NiFe LDHMs/NF, NiFe LDHMs/NF with O-vacancy (O_{vac}) formed and NiFe LDHMs/NF with re-oxidized Ni near O_{vac} were built and relaxed based the same geometry optimization algorithm. These three types of interface models were initially built with 216 atoms within the supercell and size of 26Å × 13Å × 25Å between Ni (100) and NiFe-LDHMs/NF (010). The vacuum thickness was set to the value larger than 15 Å in order to separate the other two opposite surface effect. To balance the computational demanding cost, the Monkhost-Pack reciprocal space integration was performed using Gamma-center-off special k-points with mesh of 2 × 2 × 1 [39], which was guided by the initial convergence test. With these settings, the overall total energy for each step are converged to less than 5.0×10^{-7} eV per atom. The Hellmann-Feynman forces on the atom were converged to less than 0.001 eV/Å.

The Ni, Fe, O, and H norm-conserving pseudopotentials are generated using the

OPIUM code in the Kleinman-Bylander projector form [40], and the non-linear partial core correction [41] and a scalar relativistic averaging scheme [42] were used to treat the mixed valence (Fe, Ni) spin-orbital coupling effect. We choose the projector-based ($3d$, $4s$, $4p$), ($2s$, $2p$), and ($1s$) states to reflect the valence states of Ni, Fe, O, and H atoms respectively. The RRKJ method was chosen for the optimization of the pseudopotentials [43].

Supplementary Material

Supplementary figures and tables.

Competing Interests

The authors have declared that no competing interest exists.

Funding

Author contributions

J.P.L., X.Q.H. and Z.Y.Z. conceived and designed the experiments. Z.Y.Z. carried out the catalyst synthesis and electrochemical experiments. X.X.J., J.Y.X., and X.R.C. performed SEM and TEM studies. B.L.H. performed DFT calculations. Z.Y.Z., X.Q.H., J.P.L. and B.L.H. wrote the manuscript. All authors contributed to the discussion and revision of paper.

References

1. Chu, S., Majumdar, A. Opportunities and challenges for a sustainable energy future. *Nature* **488,** 294-303 (2012).

2. Kanan, M. W., Nocera, D. G. In situ formation of an oxygen-evolving catalyst in neutral water containing phosphate and Co^{2+}. *Science* **321,** 1072-1075 (2008).

3. Sahasrabudhe, A., Dixit, H., Majee, R. & Bhattacharyya, S. Value added transformation of ubiquitous substrates into highly efficient and flexible electrodes for water splitting. *Nat. Commun.* **9,** 2014 (2018).

4. Yan, J. Q., Kong, L. Q., Ji, Y. J., White, J., Li, Y. Y., Zhang, J., An, P. F., Liu, S. Z., Lee, S. T. & Ma, T. Y. Single atom tungsten doped ultrathin α-Ni(OH)$_2$ for enhanced electrocatalytic water oxidation. *Nat. Commun.* **10,** 2149 (2019).

5. Ju, S. K., Kim, B., Kim, H., Kang, K. Recent progress on multimetal oxide catalysts for the oxygen evolution reaction. *Adv. Energy Mater.* **8,** 1702774 (2018).

6. Suntivich, J., May, K. J., Gasteiger, H. A., Goodenough, J. B., Shao-Horn, Y. A perovskite oxide optimized for oxygen evolution catalysis from molecular orbital principles. *Science* **334,** 1383-1385 (2011).

7. Fang, Y., Zhou, H. Q., Huang, Y. F., Sun, J. Y., Qin, F., Bao, J. M., Goddard Ⅲ, W. A., Chen, S., Ren, Z. F. High-performance bifunctional porous non-noble metal phosphide catalyst for overall water splitting. *Nat. Commun.* **9,** 2551, (2018).

8. Concina, I., Ibupoto, Z. H., Vomiero, A. Semiconducting metal oxide nanostructures for water splitting and photovoltaics. *Adv. Energy Mater*. **7,** 1700706 (2017).

9. Dong, C. Q., Kou, T. Y., Gao, H., Peng, Z. Q., Zhang, Z. Z. Eutectic-derived mesoporous Ni-Fe-O nanowire network catalyzing oxygen evolution and overall water splitting. *Adv. Energy Mater*. **8,** 1701347 (2017).

10. Weng, B. C., Xu, F. H., Wang, C. L., Meng, W. W., Grice, C. R., Yan, Y. F. A layered $Na_{1-x}Ni_yFe_{1-y}O_2$ double oxide oxygen evolution reaction electrocatalyst for highly efficient water-splitting. *Energy Environ. Sci.* **10,** 121-128 (2017).

11. Zhao, Y. F., Zhang, X., Jia, X. D., Waterhouse, G. I. N., Shi, R., Zhang, X. R., Zhan, F., Tao, Y., Wu, L. Z., Tung, C.-H., O'Hare, D., Zhang, T. R. Sub-3 nm ultrafine monolayer layered double hydroxide nanosheets for electrochemical water oxidation. *Adv. Energy Mater*. **8,** 1703585 (2018).

12. Fan, K., Chen, H., Ji, Y. F., Huang, H., Claesson, P. M., Daniel, Q., Philippe, B., Rensmo, H., Li, F. S., Luo, Y & Sun, L. C. Nickel-vanadium monolayer double hydroxide for efficient electrochemical water oxidation. *Nat. Commun.* **7,** 11981 (2016).

13. Meng, F. L., Zhong, H. X., Bao, D., Yan, J., Zhang, X. B. In situ coupling of strung Co_4N and intertwined N-C fibers towards free-standing bifunctional cathode for robust, efficient, and flexible Zn-Air batteries. *J. Am. Chem. Soc.* **138,** 10226-10231 (2016).

14. Liu, K. L., Wang, F. M., Shifa, T. A., Wang, Z. X., Cheng, Z. Z., Zhan, X. Y., He, J. The role of active oxide species for electrochemical water oxidation on the surface of 3d-metal phosphides. *Adv. Energy Mater.* **8,** 1703290 (2018).

15. Han, B. H., Stoerzinger, K. A., Tileli, V., Gamalski, A. D., Stach, E. A & Shao-Horn, Y. Nanoscale structural oscillations in perovskite oxides induced by oxygen evolution. *Nat. Mater.* **16,** 121-126 (2016).

16. Grimaud, A., Diaz-Morales, O., Han, B. H., Hong, W. T., Lee, Y.-L., Giordano, L., Stoerzinger, K. A., Koper, M. T. M., Shao-Horn, T. Activating lattice oxygen redox reactions in metal oxides to catalyse oxygen evolution. *Nat. Chem.* **9,** 457-465 (2017).

17. Yu, L., Yang, J. F., Guan, B. Y., Lu, Y., Lou, X. W. Hierarchical Hollow nanoprisms based on ultrathin Ni-Fe layered double hydroxide nanosheets with enhanced electrocatalytic activity towards oxygen evolution. *Angew. Chem. Int. Ed.* **130,** 178-182 (2018).

18. Li, P., Duan, X. X., Kuang, Y., Li, Y. P., Zhang, G. X., Liu, W., Sun, X. M. Tuning electronic structure of NiFe layered double hydroxides with vanadium doping toward highly efficient electrocatalytic water oxidation. *Adv. Energy Mater.* **8,** 1703341 (2018).

19. Han, L., Dong, S. J., Wang, E. Transition-metal (Co, Ni, and Fe)-based electrocatalysts for the water oxidation reaction. *Adv. Mater.* **28,** 9266-9291 (2016).

20. Chen, G. B., Wang, T., Zhang, J., Liu, P., Sun, H. J., Zhuang, X. D., Chen, M. W., Feng, X. L. Accelerated hydrogen evolution kinetics on NiFe-Layered double hydroxide electrocatalysts by tailoring water dissociation active sites. *Adv. Mater.* **30,** 1706279 (2018).

21. Yang, Y., Dang, L. N., Shearer, M. J., Sheng, H. Y., Li, W. J., Chen, J., Xiao, P., Zhang, Y. H., Hamers, R. J., Jin, S. Highly active trimetallic NiFeCr layered double hydroxide electrocatalysts for oxygen evolution reaction. *Adv. Energy Mater.* **8,** 1703189 (2018).

22. Rosen, J., Hutchings, G. S., Jiao, F. Ordered mesoporous cobalt oxide as highly efficient oxygen evolution catalyst. *J. Am. Chem. Soc.* **135,** 4516-4521 (2013).

23. Li, Y., Li, F. M., Meng, X. Y., Wu, X.-R., Li, S. N., Chen, Y. Direct chemical synthesis of ultrathin holey iron doped cobalt oxide nanosheets on nickel foam for oxygen evolution reaction. *Nano Energy.* **54,** 238-250 (2018).

24. Bai, J., Zhong, X., Jiang, S., Huang, Y., Duan, X. F. Graphene nanomesh. *Nat. Nanotechnol.* **5,** 190-194 (2010).

25. Wu, J. J., Peng, J., Yu, Z., Zhou, Y., Guo, Y. Q., Li, Z. J., Lin, Y., Ruan, K. Q., Wu, C. Z., Xie, Y. Acid-assisted exfoliation toward metallic sub-nanopore TaS_2 monolayer with high volumetric capacitance. *J. Am. Chem. Soc.* **140,** 493-498 (2018).

26. Grimaud, A., May, K. J., Carlton, C. E., Lee, Y. L., Risch, M., Hong, W. T., Zhou, J. G., Shao-Horn, Y. Double perovskites as a family of highly active catalysts for oxygen evolution in alkaline solution. *Nat. Commun.* **4,** 2439 (2013).

27. Chen, D. W., Qiao, M., Lu, Y. R., Liu, D. D., Dong, C. L., Li, Y. F., Wang, S. Y. Preferential cation vacancies in perovskite hydroxide for oxygen evolution reaction. *Angew. Chem. Int. Ed.* **57,** 8691-8696 (2018).

28. Hu, C. L., Zhang, L., Zhao, Z. J., Li, X., Chang, X. X., Gong, J. J. Synergism of geometric construction and electronic regulation: 3D Se-(NiCo)S_x/(OH)$_x$ nanosheets for highly efficient overall water splitting. *Adv. Mater.* 30, 1705538 (2018).

29. Zhao, Y. F., Jia, X. D., Chen, G. B., Shang, L., Waterhouse, G. I. N., Wu, L. Z., Tung, C. H., O'Hare, D., Zhang, T. R. Ultrathin NiO nanosheets stabilized by TiO_2 from monolayer NiTi-LDH precursors: an active water oxidation electrocatalysts. *J. Am. Chem. Soc.* **138,** 6571-6524 (2016).

30. Radich, J. G., Kamat, P. V. Making graphene holey gold-nanoparticle-mediated hydroxyl radical attack on reduced graphene oxide. *ACS Nano.* **7,** 5546-5557 (2013).

31. Tang, C., Wang, H. S., Wang, H. F., Zhang, Q., Tian, G. L., Nie, J. Q., Wei, F. Spatially confined hybridization of nanometer-sized NiFe hydroxides into nitrogen-doped graphene frameworks leading to superior oxygen evolution reactivity. *Adv. Mater.* **27,** 4516-4522 (2015).

32. Suryawanshi, M. P., Ghorpade, U. V., Shin, S. W., Suryawanshi, U. P., Jo, E., Kim, J. H. Hierarchically coupled Ni:FeOOH nanosheets on 3D N-doped graphite foam as self-supported electrocatalysts for efficient and durable water oxidation. *ACS Catal.* **9,** 5025-5034 (2019).

33. Wang, Y. Y., Qiao, M., Li, Y. F., Wang, S. Y. Tuning surface electronic configuration of NiFe LDHs nanosheets by introducing cation vacancies (Fe or Ni) as highly efficient electrocatalysts for oxygen evolution reaction. *Small.* **14,** 1800136 (2018).

34. Liang, Y. Y., Wang, H. L., Zhou, J. G., Li, Y. Y., Wang, J., Regier, T., Dai, H. J. Covalent hybrid of spinel manganese-cobalt oxide and graphene as advanced oxygen reduction electrocatalysts. *J. Am. Chem. Soc.* **134,** 3517-3523 (2012).

35. Zhuang, L. Z., Ge, L., Yang, Y. S., Li, M. R., Jia, Y., Yao., X. D., Zhu, Z. H. Ultrathin iron-cobalt oxide nanosheets with abundant oxygen vacancies for the oxygen evolution reaction. *Adv. Mater.* **29,** 1606793 (2017).

36. Wan, K., Luo, J. S., Zhou, C., Zhang, T., Arbiol, J., Lu, X. H., Mao, B. W., Zhang, X., Fransaer, J. Hierarchical porous Ni_3S_4 with enriched high-valence Ni sites as a robust electrocatalyst for efficient oxygen evolution reaction. *Adv. Funct. Mater.* **29,** 1900315 (2019).

37. Clark, S. J., Segall, M. D., Pickard, C. J., Hasnip, P. J., Probert, M. J., Refson, K., Payne, M. C. First principles methods using CASTEP. *Zeitschrift Fur Kristallographie* **220,** 567-570 (2005).

38. Marzari, N., Vanderbilt, D., Payne, M. C. Ensemble density-functional theory for *ab initio* molecular dynamics of metals and finite-temperature insulators. *Phys. Rev. Lett.* **79,** 1337-1340 (1997).

39. Probert, M. I. J., Payne, M. C. Improving the convergence of defect calculations in supercells: an *ab initio* study of neutral silicon vacancy. *Phys. Rev. B* **67,** 075204 (2003).

40. Kleinman, L., Bylander, D. M. Efficacious form for model pseudopotentials. *Phys. Rev. Lett.* **48,** 1425-1428 (1982).

41. Louie, S. G., Froyen, S., Cohen, M. L. Nonlinear ionic pseudopotentials in spin-density-functional calculations. *Phys. Rev. B* **26,** 1738-1742 (1982).

42. Grinberg, I., Ramer, N. J., Rappe, A. M. Transferable relativistic dirac-slater pseudopotentials. *Phys. Rev. Lett.* **62,** 2311-2314 (2000).

43. Rappe, A. M., Rabe, K. M., Kaxiras, E., Joannopoulos, J. D. Optimized pseudopotentials. *Phys. Rev. Lett.* **41,** 1227-1230 (1990).
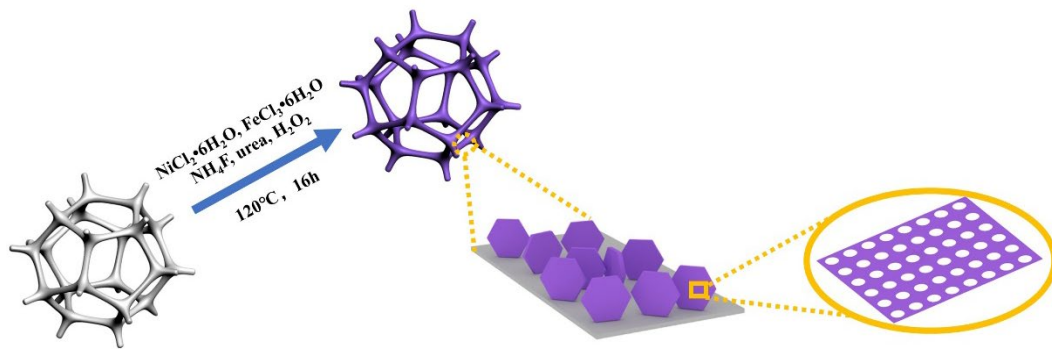
Figures

Fig. 1 │Schematic illustration of the synthetic process of NiFe LDHMs/NF.
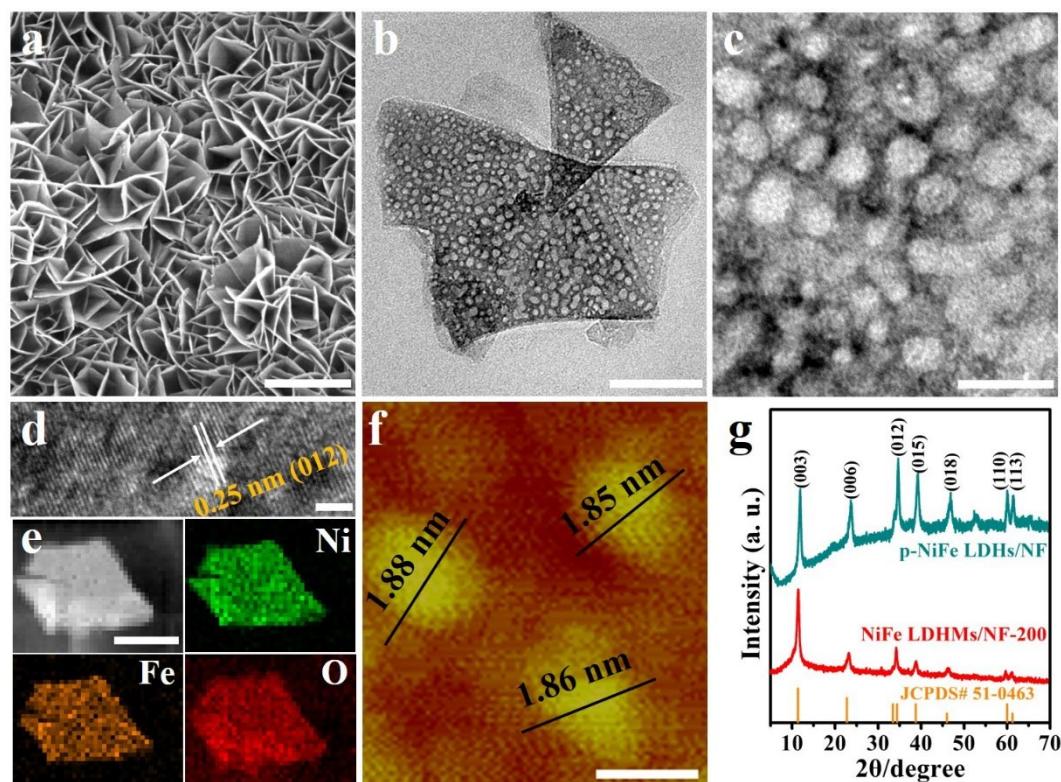
Fig. 2│Morphological and structural characterizations. (a) SEM image of NiFe LDHMs/NF-200. **(b)** low-magnification and **(c)** high-magnification TEM images of NiFe LDHMs-200 scratched off from NF. **(d)** HRTEM image of NiFe LDHMs-200 scratched off from NF. **(e)** Typical HAADF-STEM image and its corresponding EDX elemental mapping images of NiFe LDHMs-200 scratched off from NF. **(f)** AFM image of NiFe LDHMs-200 scratched off from NF. **(g)** PXRD patterns p-NiFe LDHs and NiFe LDHMs-200 scratched off from NF. Scale bar: **(a)** 2 μm; **(b)** 100 nm; **(c)** 20 nm; **(d)** 2 nm; **(e)** 100 nm; **(f)** 50 nm.
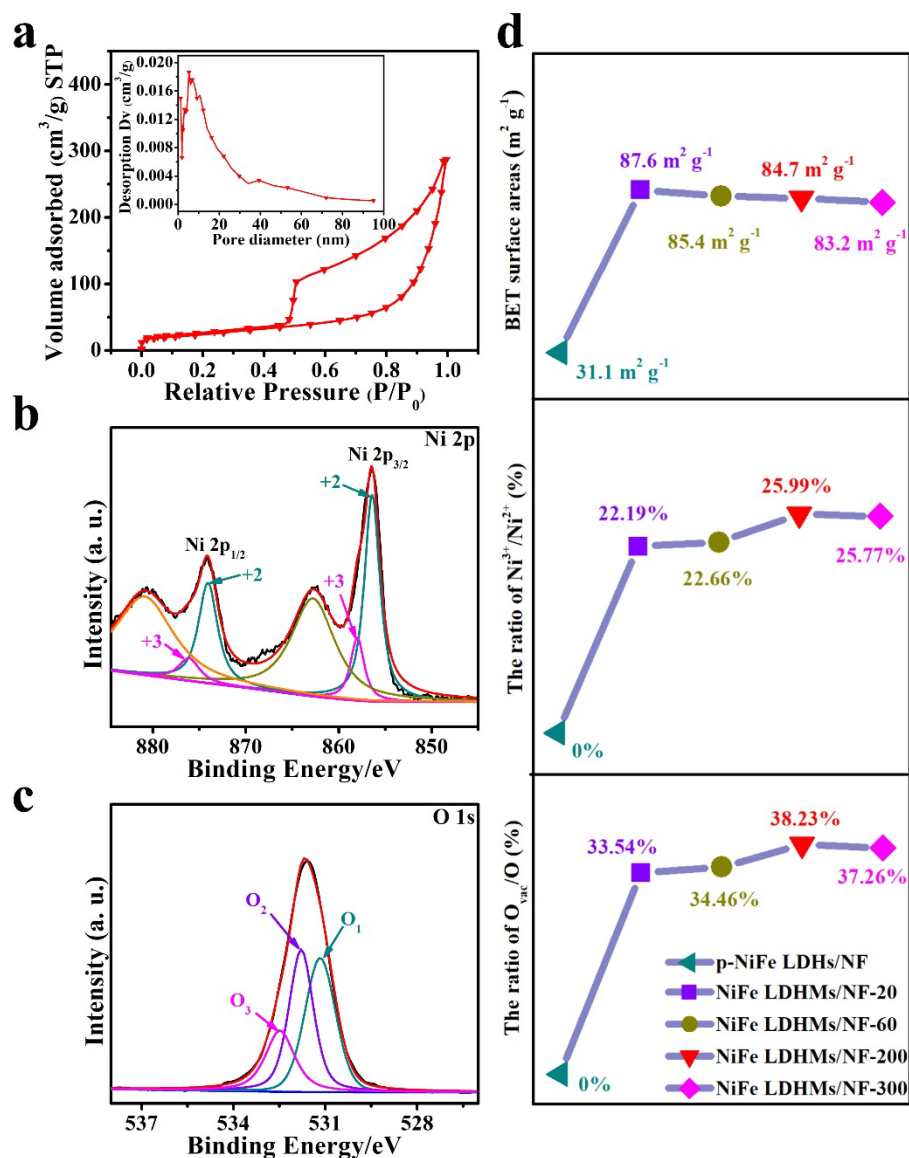
Fig. 3 │ BET surface area and XPS characterizations. (a) N_2 absorption-desorption isotherms of NiFe LDHMs/NF-200. Inset **(a)** is the corresponding pore size distribution. High-resolution XPS spectra of **(b)** Ni 2p, **(c)** O 1s regions of NiFe LDHMs/NF-200, respectively. **(d)** BET surface areas, the ratios of Ni^{2+}/Ni^{3+} and O_{vac}/O of NiFe LDHMs/NF treated with different amounts of H_2O_2.
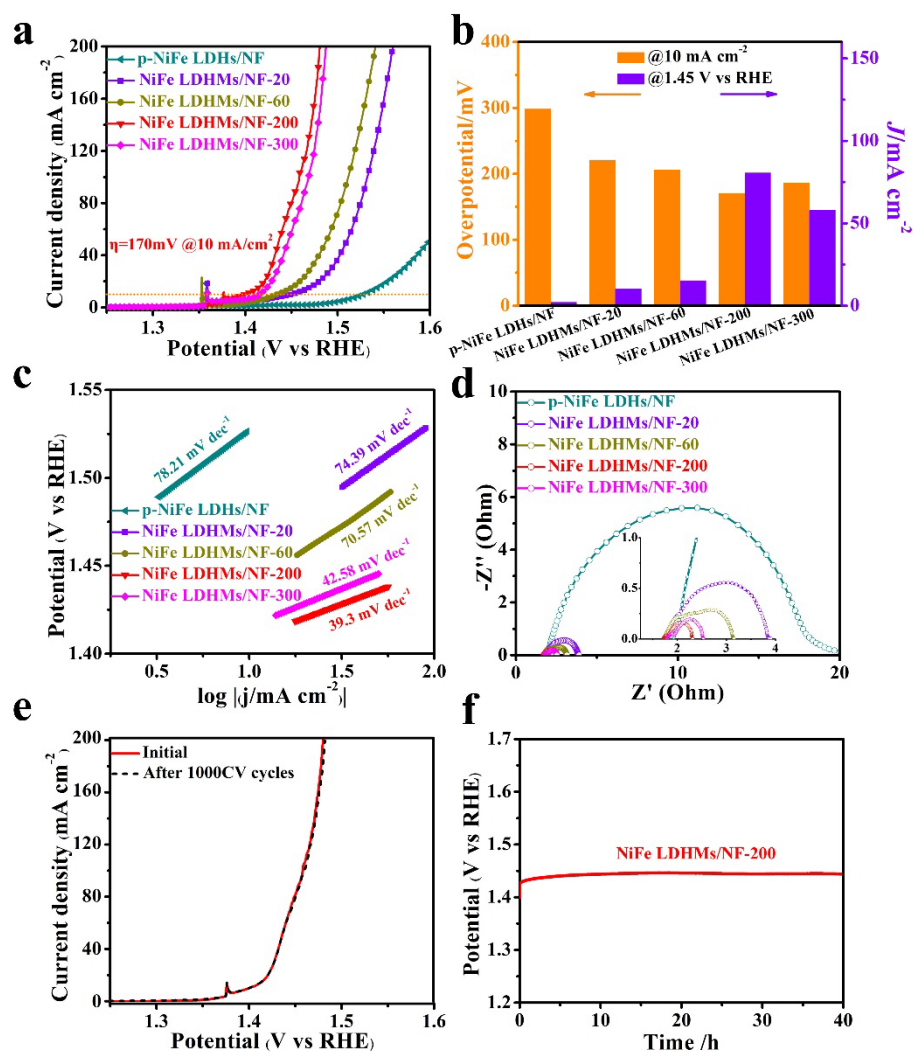
Fig. 4 │ Electrochemical OER performance. (a) Polarization curves recorded on different electrocatalysts at a scan rate of 5 mV s^{-1} in 1 M KOH with 95% *iR*-compensation. **(b)** The current density at 1.45 V (vs. RHE) and overpotential at 10 mA cm^{-2}. **(c)** The corresponding Tafel plots. **(d)** EIS spectra of the samples. **(e)** Polarization curves of NiFe LDHMs/NF-200 before and after 1000 CV cycles. **(f)** Chronopotentiometry curve of NiFe LDHMs/NF-200 at a current density of 10 mA cm^{-2}.
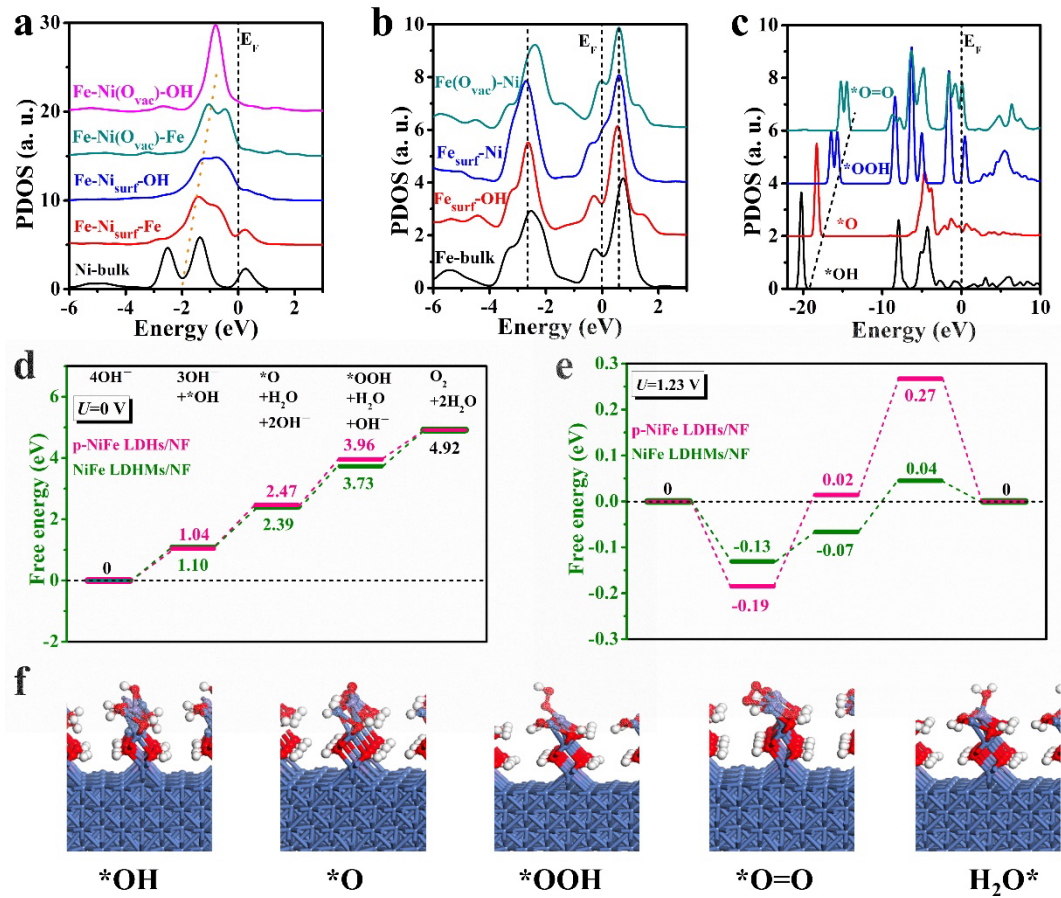
Fig. 5 │ DFT calculation on improving OER performance of NiFe LDHMs/NF. (a) PDOSs of Ni-3d bands from deep bulk region (Ni-bulk), towards surface Ni bonded with Fe-sites (Fe-Ni$_{surf}$-Fe), surface Ni bonded with Fe and OH (Fe-Ni$_{surf}$-OH), surface edge Ni-sites near O$_{vac}$ bonded with Fe-sites (Fe-Ni(O$_{vac}$)-Fe) and surface edge Ni-site near O$_{vac}$ bonded with Fe and OH (Fe-Ni(O$_{vac}$)-OH), respectively. **(b)** PDOSs of Fe-3d bands from deep bulk region (Fe-bulk) towards surface site bonded with OH (Fe$_{surf}$-OH), surface site bonded with Ni (Fe$_{surf}$-Ni) and edge site near O$_{vac}$ (Fe(O$_{vac}$)-OH). **(c)** PDOSs of O-2p bands for the intermediate O-species. **(d)** The free energy diagrams for OER on p-NiFe LDHs/NF and NiFe LDHMs/NF at zero potential (U=0 V). **(e)** The free energy diagrams for OER on p-NiFe LDHs/NF and

NiFe LDHMs/NF at equilibrium potential (U=1.23 V). **(f)** Local structural configurations of initial reactant, intermediates or final product on the NiFe LDHMs/NF with Ni re-oxidized near O_{vac}. The purple, blue, red and white atoms represent the Ni, Fe, O and H.